Vesicle Deformation by an Axial Load: From Elongated Shapes to Tethered Vesicles

Volkmar Heinrich,* Bojan Božič,* Saša Svetina,*§ and Boštjan Žekš*§
*Institute of Biophysics, Medical Faculty, Lipičeva 2, University of Ljubljana, and §J. Stefan Institute, Jamova 39, SI-1000 Ljubljana, Slovenia

ABSTRACT A sufficiently large force acting on a single point of the fluid membrane of a flaccid phospholipid vesicle is known to cause the formation of a narrow bilayer tube (tether). We analyze this phenomenon by means of general mathematical methods allowing us to determine the shapes of strongly deformed vesicles including their stability. Starting from a free vesicle with an axisymmetric, prolate equilibrium shape, we consider an axial load that pulls (or pushes) the poles of the vesicle apart. Arranging the resulting shapes of strained vesicles in dependence of the axial deformation and of the area difference of monolayers, phase diagrams of stable shapes are presented comprising prolate shapes with or without equatorial mirror symmetry. For realistic values of membrane parameters, we study the force–extension relation of strained vesicles, and we demonstrate in detail how the initially elongated shape of an axially stretched vesicle transforms into a shape involving a membrane tether. This tethering transition may be continuous or discontinuous. If the free vesicle is mirror symmetric, the mirror symmetry is broken as the tether forms. The stability analysis of tethered shapes reveals that, for the considered vesicles, the stable shape is always asymmetric (polar), i.e., it involves only a single tether on one side of the main vesicle body. Although a bilayer tube formed from a closed vesicle is not an ideal cylinder, we show that, for most practical purposes, it is safe to assume a cylindrical geometry of tethers. This analysis is supplemented by the documentation of a prototype experiment supporting our theoretical predictions. It shows that the currently accepted model for the description of lipid-bilayer elasticity (generalized bilayer couple model) properly accounts for the tethering phenomenon.

INTRODUCTION

A point-force acting on the fluid membrane of a flaccid phospholipid vesicle is known to pull out a narrow bilayer tube (tether) from the vesicle membrane (Waugh, 1982). A variety of experimental techniques using tether formation have been developed and have substantially increased our knowledge about the mechanical properties of lipid membranes. For example, tether-pulling experiments provided accurate values for the local bending modulus of fluid bilayers (Bo and Waugh, 1989; Song and Waugh, 1993; Heinrich and Waugh, 1996), and they also allowed for the first measurements of the nonlocal bending modulus (Waugh et al., 1992; Raphael and Waugh, 1996). Furthermore, the interlayer drag coefficient characterizing the frictional interaction between the two membrane leaflets when sliding past each other was measured by tether formation (Evans and Yeung, 1994). Recent long-term observations of slowly growing membrane tethers could be interpreted by postulating an elastically driven, accelerated flip-flop of lipids from the inner to the outer monolayer (Raphael and Waugh, 1996; Svetina et al., 1998). Other sets of recent experiments involved tethers that were caused by internal structures like microtubules growing inside vesicles (Hotani and Miyamoto, 1990; Kuchnir Fygenson et al., 1997a, 1997b; Umeda et al., 1998). Beside these studies of artificial lipid membranes, a number of tether experiments have been performed using biological cells, revealing new insight in cell membrane elasticity (e.g., Hochmuth et al., 1973, 1982, 1996; Dai and Sheetz, 1995). Recently, tethers pulled from red blood cells provided a measurement of the interaction strength between the plasma membrane and the underlying protein network (Waugh and Bauserman, 1995; Hwang and Waugh, 1997).

In these experiments, the measurements are usually carried out when tubular membrane extensions of sufficient length have already formed. Variation of the tether width or the tether length provides the desired mechanical deformation. For the interpretation of measurements, it is generally assumed that the (often invisible) tether has a cylindrical shape, and simple parametrical models are used to extract the values of different membrane material constants from the measured data. The experience from a large number of experiments, and the often good agreement of the measured data with predictions of the parametrical models indicate that the used procedures are sufficiently accurate to fulfill the purpose that they were designed for. Yet the fundamental questions why and how tethers form in the first place are not addressed by these models. The interesting task to reveal the basic mechanisms of tether formation is left to studies using more general mathematical methods and, most likely, involving nontrivial numerical computations.

Received for publication 20 February 1998 and in final form 7 December 1998.

Address reprint requests to Bojan Božič, Institute of Biophysics, Medical Faculty, University of Ljubljana, Lipičeva 2, SL-1000 Ljubljana, Slovenia. Tel.: 38661 314 127; Fax: 38661 131 5127; E-mail: bojan.bozic@biofiz.mf.uni-lj.si.

Dr. Heinrich's present address is Department of Physics and Astronomy, University of British Columbia, 6224 Agricultural Road, Vancouver, British Columbia V6T 1Z1, Canada.

0006-3495/99/04/2056/16 $2.00

Such studies can be based on the existing broad knowledge about the shapes of free flaccid vesicles. The shape variety of unsupported lipid vesicles has been the subject of elaborate theoretical and experimental research work (reviewed e.g., in Lipowsky, 1991; Sackmann, 1995; Svetina and Žekš, 1996; Seifert, 1997). A continuum mechanical model accounting for the double-layer structure of the membranes of artificial phospholipid vesicles ("generalized bilayer couple model", Evans, 1974; Svetina et al., 1992; Seifert et al., 1992; Božič et al., 1992; Wiese et al., 1992; Heinrich et al., 1993) has been able to reproduce many experimental observations quite reasonably (e.g., Käs et al., 1993; Miao et al., 1994; Wintz et al., 1996; Döbereiner et al., 1997), and a general picture of the shape behavior of free vesicles is emerging. Naturally, the theoretical work was accompanied by the development of mathematical methods for the appropriate description of closed surfaces exhibiting the elastic properties of simple bilayer membranes.

Only very recently, some of these tools were applied also to the shapes of axially strained vesicles. Considering the stability of the cylindrical section of a pipette-aspirated, tethered vesicle, it was shown that the existence of tethers is consistent with the generalized bilayer couple model (Bukman et al., 1996). Starting more generally from the well-known equilibrium shapes of axisymmetric free vesicles, it is instructive to consider axial loads that pull or push the vesicle poles apart. Modeling this situation, a preceding study (Božič et al., 1997) was devoted to the physics of membrane deformations caused by a force acting in one point, and to the specification of an Euler–Lagrange variational procedure for this case. However, concentrating primarily on the basic mechanisms of the onset of tether formation, the calculations in that study were restricted to prolate axisymmetric vesicle shapes containing a mirror plane at the equator. Moreover, the stability of stationary shapes was not analyzed, and numerical problems had limited the range of considered deformations to moderate vesicle extensions. In the present paper, we extend the analysis by allowing also for shapes with broken equatorial mirror symmetry, and we show that these shapes actually dominate the shape behavior of axially strained vesicles. Furthermore, the Euler–Lagrange variational procedure used previously is now supplemented by a Ritz method that we recently developed to describe strongly deformed vesicle shapes. The combination of these two methods has enabled us to study considerably larger deformations than before, and to include a stability analysis of stationary shapes. With these improvements, we may now systematically explore the shapes and shape transformations of axisymmetric, axially strained vesicles. Although the theoretical background as well as the basic mechanisms presented earlier remain fully applicable, we are now able to specify the predictions for related experiments more precisely. Performing the numerical calculations for a realistic range of material parameters of phospholipid membranes, the present results should be directly applicable to experimental situations. Finally, we suggest a new experiment and document a prototype version of it that has partially inspired the present theoretical study.

The paper is organized as follows. The next section gives an overview of the generalized bilayer couple model, i.e., of the elastic energy contributions that determine the shape of a simple bilayer membrane, and of the relevant constraints. The model specifications for axially strained vesicles and the mathematical methods used to tackle the resulting variational problem are explained in the following two sections. Eventually, numerical results are presented and discussed. The conclusions emphasize the implications of our results for related experiments.

GENERALIZED BILAYER COUPLE MODEL

In general, the shapes of flaccid vesicles are governed by the elastic energy of the vesicle membrane. It is the sum of the local and the nonlocal bending energy (Helfrich, 1973; Evans, 1974, 1980; Božič et al., 1992; Miao et al., 1994) and reads, for symmetrical bilayers,

$$W_{\mathrm{el}} = W_{\mathrm{b}} + W_{\mathrm{r}} = \frac{k_{\mathrm{c}}}{2}\int (C_1 + C_2)^2 \,\mathrm{d}A + \frac{k_{\mathrm{r}}}{2A}\left(\frac{\Delta A - \Delta A_0}{h}\right)^2. \tag{1}$$

The local bending energy W_{b} is the integral of the squared sum of the two principal curvatures C_1 and C_2 over the closed surface area A, multiplied by the local bending modulus k_{c}. The nonlocal bending energy W_{r} is the energy of relative stretching of the two layers with respect to each other. The difference between the areas of the two layers is given by

$$\Delta A = h\int (C_1 + C_2)\,\mathrm{d}A, \tag{2}$$

where h is the distance between the neutral surfaces of the layers. The equilibrium value of the area difference ΔA_0 is defined for isolated monolayers. It depends on the numbers of lipid molecules constituting the layers and on the (relaxed) area per molecule. The nonlocal bending modulus is denoted by k_{r}.

The value of the nonlocal bending modulus k_{r} can be easily estimated to be a few times the value of the local bending modulus k_{c} (Waugh et al., 1992). Therefore, vesicle deformations are generally accompanied by comparable changes in both the local as well as the nonlocal bending energy. Yet, although name and definition of the nonlocal bending energy first appeared quite some time ago (Evans, 1974, 1980; Helfrich, 1974), its importance in the mechanics of layered membranes has long been overlooked. The different models of vesicle shapes that have been suggested and studied during the past two decades were mainly distinguished by the value used for k_{r}, with values ranging from zero to infinity (e.g., Deuling and Helfrich, 1976; Svetina and Žekš, 1989; Seifert et al., 1991; Heinrich et al., 1992). We emphasize that it was tether formation that

answered the question which of the existing vesicle-shape models is most adequate to describe experimental observations (Božič et al., 1992). The first measurements of the nonlocal bending modulus k_r by means of tether formation (Waugh et al., 1992) provided also a quantitative verification of the generalized bilayer couple model, which is based on the energy expression given in Eq. 1. (For an early account of the history of this model, see the Introduction of Heinrich et al., 1993.) Recently, it was demonstrated that the study of vesicle shape fluctuations could also serve to test this model quantitatively (Döbereiner et al., 1995, 1997). The latter works adhere to the notion of the area-difference elasticity model (synonym to generalized bilayer couple model) that was developed independently (Seifert et al., 1992; Miao et al., 1994) to improve the understanding of the budding shape transition of free vesicles. It should be noted that, in that model, the material parameter characterizing the nonlocal bending energy is defined as k_r/π.

To determine the equilibrium shape of a free vesicle, one has to minimize the elastic energy given in Eq. 1. Because the membrane tensions of free vesicles as well as of the strained vesicles considered here are always small compared to tensions that would cause a significant change of the membrane area A, we may take the area to be constant. Not allowing for changes in the osmolarity of the solution surrounding the vesicle, the vesicle volume V is also fixed. Therefore, the energy minimization has to be performed at constant values of these constraints. Stationary shapes are characterized by a vanishing first variation of the energy functional that includes the constraints via Lagrange multipliers. To decide whether a stationary shape corresponds to a minimum of the elastic energy, an appropriate stability analysis has to be performed.

The resulting equilibrium shapes of free vesicles have been arranged in a $V - \Delta A_0$ phase diagram of stable shapes, which is in reasonable agreement with experimental observations (Heinrich et al., 1993; Miao et al., 1994; Jarić et al., 1995). The two main regions of this phase diagram contain prolate and oblate axisymmetric shapes, respectively. Either region is further divided into subregions of shapes with or without equatorial mirror symmetry. Except for vesicles with very low volume-to-area ratios (Wintz et al., 1996), it has been shown that, for realistic values of the ratio k_r/k_c, nonaxisymmetric shapes are generally of little or no relevance as stable equilibrium shapes (Heinrich et al., 1993; Jarić et al., 1995).

VESICLE DEFORMATION BY AXIAL STRAIN

Based on the knowledge about unsupported vesicles, we study the following physical situation. Starting from a free vesicle with a known equilibrium shape, we consider two points of the vesicle surface that are moved apart by a force acting on these two points. The force may be a pulling force acting on the outside of the vesicle, or a pushing force exerted by an internal structure. Because the lipid bilayer is fluid, the vesicle initially will merely change its orientation until the two points span the largest possible distance between any two points of the vesicle surface. This reorientation does not cost energy, i.e., it takes place at infinitesimal force. Any further increase of the distance between the two points changes the vesicle shape and requires a finite force. If the free vesicle has a prolate axisymmetric equilibrium shape, the force will thus eventually act along the symmetry axis and pull the poles of the vesicle apart. We do not expect this deformation to affect the rotational symmetry of the vesicle. In the case of an oblate shape, however, the force will act on two points of the largest cross section perpendicular to the symmetry axis, and so, it will cause a nonaxisymmetric deformation. Yet even in this case, it seems likely that sufficiently high forces will eventually cause the deformed vesicle to become axisymmetric. However, the theoretical treatment of this case is considerably more difficult and is beyond the scope of this study. Considering only prolate shapes, the present analysis stays within the case of rotational symmetry of free as well as of axially strained vesicles.

Principally, there are two different ways to impose the axial vesicle deformation considered here. They can be studied experimentally using the techniques presented as prototype versions in Figs. 1 and 2. It is important to note that these two cases correspond to different thermodynamic potentials (cf. Fig. 3). In the first scenario, the vesicle poles are clamped at two points separated by a fixed distance (Figs. 1 and 3 *A*). Experimentally, this can be achieved by using the (often unwanted) property of lipid membranes to adhere to glass surfaces. Attaching a vesicle membrane to the tips of two glass micropipettes (Fig. 1) allows us to set the desired pole-to-pole distance Z and to monitor the equilibrium shapes that the vesicle assumes at different given values of Z. In this first scenario, the constant pole-to-pole distance enters the theoretical description as an additional constraint. It is incorporated in the calculations via an adjustable Lagrange multiplier representing the force that maintains this distance. The total energy is then identical with the membrane's elastic energy. Alternatively, we may consider a constant force acting on the poles, and a variable pole-to-pole distance that depends on the value of this force (Figs. 2 and 3 *B*). In the experimental example shown in Fig. 2, the applied magnetic field sets the force that the paramagnetic bead exerts at the free vesicle pole. Increasing the force results in longer axial vesicle extensions, which eventually leads to the formation of a narrow membrane tether (invisible in Fig. 2) connecting the lemon-shaped main vesicle body with the pipette tip. (Details of the experimental setup including a possible accurate measurement of the applied forces in the range of piconewtons can be found in Heinrich and Waugh, 1996.) In the thermodynamic description of this case, the work done by the force contributes to the system's total energy, and it has to be included in the energy minimization (Podgornik et al., 1995; Božič et al., 1997). The potential energy due to the axial

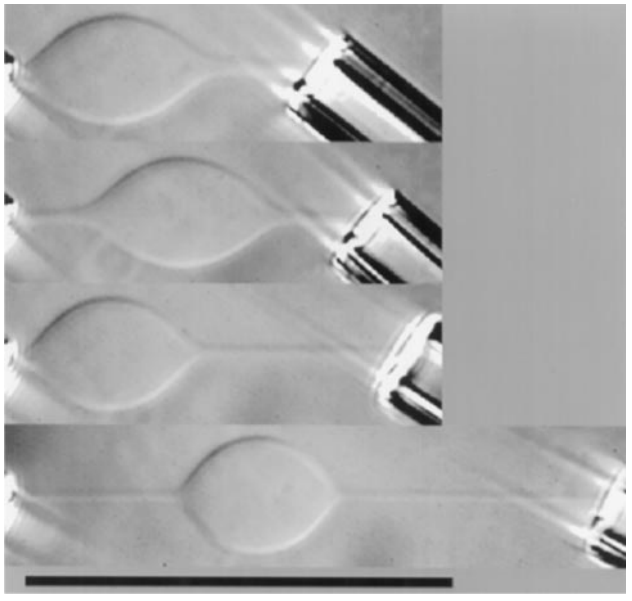

FIGURE 1 Series of four video micrographs of a phospholipid vesicle whose membrane was point-attached to the tips of two glass micropipettes. The elongated vesicle consists of tubular sections (membrane tethers) and a lemon-shaped main body. At increasing distance between the pipette tips the tether width reduces, and the main vesicle body becomes more spherical. The main body is usually located on one side of the strained vesicle. In the second picture, it was forced into the vesicle's center by applying a directed flow through the left pipette for a short time. Similarly, the bottom shape involving two tethers resulted from a rapid increase of the vesicle's pole-to-pole distance by simultaneously moving both pipettes away from the main body. Alignment of the Hoffman optics and contrast enhancement due to the different refraction indices of different sugar solutions in- and outside the vesicle allowed us to make the tethers visible. The horizontal bar corresponds to 50 μm.

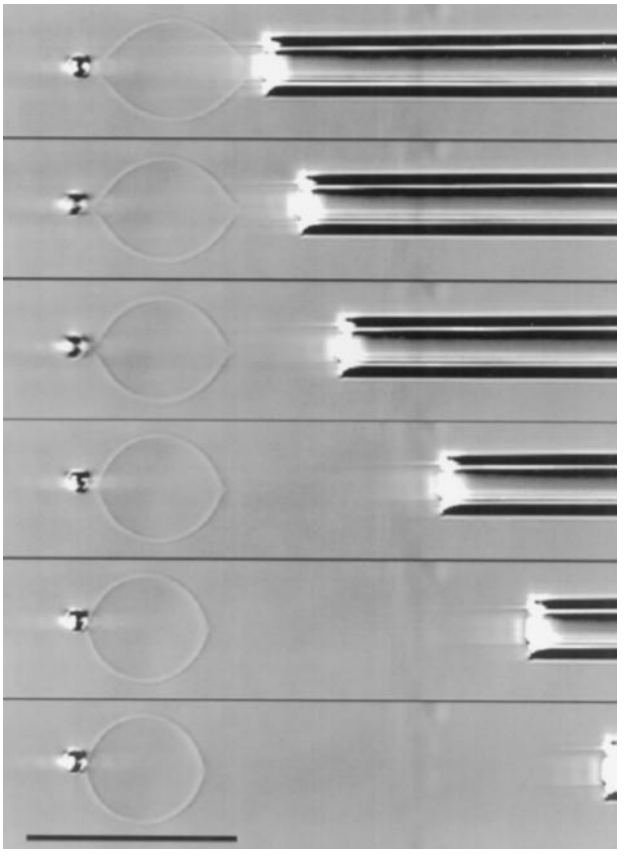

FIGURE 2 Series of video micrographs of a phospholipid vesicle whose membrane was point-attached on one side to the tip of a glass micropipette and on the other side to a paramagnetic bead. An electromagnet was used to apply increasing pulling forces to the vesicle (*top* to *bottom*). Once the equilibrium vesicle extension had established, the pipette was moved backward to place the bead at a predefined horizontal position. The tether connecting the main vesicle body and pipette tip in the lower five pictures is too thin to be resolved by light microscopy. The same aqueous solution was used in- and outside the vesicle to avoid an asymmetry that could cause a non-negligible spontaneous curvature of the lipid bilayer. An independent measurement of the local bending modulus k_c was carried out for this vesicle and proved that it was unilamellar. The horizontal bar corresponds to 50 μm.

force is simply

$$W_f = -FZ, \tag{3}$$

where F denotes the axial force, and Z is the pole-to-pole distance of the vesicle shape. The stationary shapes corresponding to these two scenarios are the same. However, their stability, as well as the character of shape transitions, may be different in the two cases.

VARIATIONAL PROCEDURES

The variational problem of minimizing the total energy in the presence of constraints is tackled with two different mathematical methods. The first is the usual Euler–Lagrange formalism that requires us to solve a higher-order Euler differential equation. Second, we present a new Ritz method (cf. e.g., Courant and Hilbert, 1924) that expands the vesicle shape in a series of basis functions and searches for those values of expansion coefficients that minimize the energy and fulfill the constraints. The general theoretical background and technical details of the application of the Euler–Lagrange procedure to the problem of axially strained vesicles have been explained in Božič et al. (1997) and shall not be repeated here. As an exception, we recall an interesting analytical result of the Euler–Lagrange formalism. Proper treatment of the boundary conditions revealed that a finite force acting on a single point of the vesicle membrane leaves the vesicle contour, as well as its first derivative, continuous (smooth) at this point. The principal curvatures, however, show a logarithmic divergence (Podgornik et al., 1995). Technically, this discontinuity is taken care of by an expansion of the Euler differential equation at the poles. The resulting two-point boundary value problem is solved numerically by a shooting-to-a-fitting-point algorithm. Unfortunately, for larger deformations, this method becomes extremely sensitive to the initial guesses of adjustable parameters, and it usually fails already at quite moderate values of the pole-to-pole distance. An additional deficiency is the lack of a simple stability analysis of stationary shapes within this Euler method. The Ritz

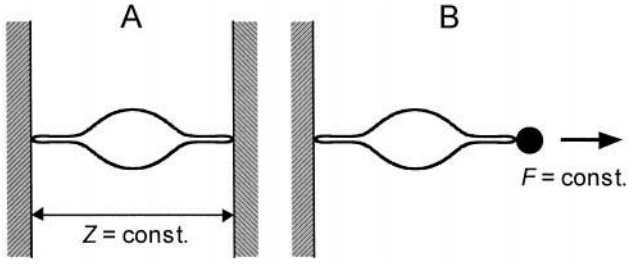

FIGURE 3 Sketches of the two scenarios corresponding to different thermodynamic ensembles. (*A*) The first is called "constant-*z* scenario." The vesicle poles are attached to fixed points, so that the vesicle assumes its equilibrium shape at a given pole-to-pole distance *Z* (cf. Fig. 1). (*B*) Alternatively, in the "constant-*f* scenario" the pole-to-pole distance is variable. Its equilibrium value depends on the (given) force acting on the vesicle poles. As is often the case in experiments (cf. Fig. 2), the force acting on the free vesicle pole is exerted by a bead (*filled circle*) in this sketch. Note that the contour of the axisymmetric vesicle (with the symmetry axis oriented horizontally) included in this graph was obtained as a stationary solution of the model presented in this paper. Its volume-to-area ratio was chosen (by eye) corresponding to that of the vesicle shown in Fig. 1.

method has enabled us to overcome most of these difficulties. Its main drawback is that it is an approximate method. However, its accuracy can always be tuned by the number of terms included in the shape expansion, and by a suitable parametrization of the shape. Furthermore, the accuracy of the Ritz method can be easily tested by comparing the results of this method with those of the Euler–Lagrange formalism in the range of vesicle extensions where both methods work.

The application of direct variational methods such as the Ritz method to vesicle shape calculations is not new (see e.g., Heinrich et al., 1992, 1993). A previously used Ritz method expanded the radial distance between the vesicle surface and the origin of the coordinate system (suitably chosen inside the vesicle) in a series of spherical harmonics. Accordingly, the independent variables of the shape parametrization were the spherical angles. That method has proven to be a powerful tool to determine the equilibrium shapes of free vesicles of arbitrary symmetry including their stability (Heinrich et al., 1993), and it also has provided new insight in the effects of thermal shape fluctuations on the vesicle shape (Heinrich et al., 1997). However, it has performed poorly when applied to the elongated shapes studied here because, at increasing pole-to-pole distance, these shapes more and more tend toward (and eventually turn into) shapes that are not anymore single-valued functions of the spherical angles. We have therefore developed a new approach (considering for now only axisymmetric shapes) that is based on a parametrization more suitable for strongly deformed vesicles. Because the contour of a vesicle is always a single-valued function of the arc length measured along the contour line, this arc length is the most practical choice for the independent variable. It turned out to be convenient to take the direction of the contour normal (i.e., the angle between the normal and a reference direction) as the dependent variable. This choice has provided a surprisingly robust way to determine the axially stretched shapes of interest. Technical details of this Ritz method are rather subtle and will be published elsewhere.

The results presented in the following were obtained by a combination of the Euler–Lagrange approach and the Ritz method. Less deformed vesicle shapes were mainly calculated by the more accurate numerical integration of the Euler differential equation. At the same time, these shapes were used to check the reliability of the Ritz method. We found that including the first 100 terms of the shape expansion in the Ritz method yielded results that were, in all checked cases, indistinguishable from the results of the Euler method. If not stated otherwise, we continued to use this number of terms when calculating the more strongly deformed shapes that are inaccessible by the Euler approach.

The constraints of constant membrane area and vesicle volume generally complicate the stability analysis of stationary shapes within the Euler method. For all shapes calculated within the Ritz method, we have determined the local stability with respect to those (axisymmetric) deformations that conserve the constraints using an improved version (see Heinrich et al., 1997) of the formalism developed originally in Heinrich et al. (1992).

RESULTS AND DISCUSSION

Dimensionless quantities

Inspection of Eq. 1 shows that the elastic energy is scale-invariant, i.e., the equilibrium shapes do not depend on the actual size of the vesicle. We may use this property to present our results in a general, dimensionless fashion (cf. e.g., Heinrich et al., 1993). As usual, we take the characteristic vesicle size to be the radius R_S of the sphere having the same surface area as the vesicle. We introduce dimensionless quantities by a normalization with respect to this sphere. To distinguish normalized quantities from the respective original ones, we denote the normalized quantities by small letters. Thus, for example, $v \equiv V/(\frac{4}{3}\pi R_S^3)$ (relative vesicle volume), $a = 1 \equiv A/(4\pi R_S^2)$ (relative surface area), $\Delta a \equiv \Delta A/(8\pi h R_S)$ (relative area difference of monolayers), $z \equiv Z/R_S$ (dimensionless pole-to-pole distance), and so on. The normalized elastic energy w_{el} is measured in units of the bending energy of a sphere ($8\pi k_c$). With this, the relative nonlocal bending energy becomes $w_r = q(\Delta a - \Delta a_0)^2$, where q is the ratio between the nonlocal and the local bending modulus, $q \equiv k_r/k_c$. The dimensionless axial force is defined as $f \equiv FR_S/(8\pi k_c)$ (cf. Božič et al., 1997).

Phase diagram of stationary shapes ($q \to \infty$)

For the presentation of numerical results, it is useful first to give a transparent overview of the relevant stationary shapes. This can be achieved by arranging the stationary shapes according to their geometrical characteristics into phase diagrams, ensuring that similar shapes occupy adja-

cent locations in these diagrams. The membrane area $a = 1$ is the same for all shapes due to the normalization. Thus, the stationary shapes of free vesicles may be characterized by the relative volume v and the relative area difference Δa. It is important to realize, however, that, unlike the constrained vesicle volume, Δa may change when a vesicle deforms, as it represents the average curvature of the vesicle shape (cf. Eq. 2). Its value can be determined by solving the variational problem at given values of v and Δa_0. Naturally, the resulting equilibrium value of Δa depends on the ratio q between the nonlocal and the local bending modulus. Choosing different values for q, however, has the mere effect of remapping a given stationary shape (with known Δa) to a new value of Δa_0, whereas the overall catalog of stationary shapes is not affected by the value of q. In other words, if we consider two distinct vesicle populations with membranes characterized by different values of q, we will find that any stationary shape obtained for one population will also be a stationary shape for the other population. However, the Δa_0 values of two vesicles having the same stationary shape will generally be different if the two vesicles belong to different populations. This applies both to unsupported vesicles (Heinrich et al., 1993) as well as to axially strained vesicles (Božič et al., 1997).

The fact that the catalog of stationary shapes does not depend on q allows us to classify the stationary shapes in a general manner. For this, we first choose q to be infinitely large. In practice, this means that the nonlocal bending energy is replaced by a constraint enforcing $\Delta a = \Delta a_0$. Then, the two constrained geometrical parameters v and Δa map the resulting stationary shapes of free vesicles into a two-dimensional phase diagram. Unfortunately, the phase diagram of stationary shapes of axially strained vesicles is three-dimensional, with the pole-to-pole distance z as the third parameter. For relative volumes not too small, however, we expect the general shape behavior to be similar at different volumes. To study this behavior qualitatively, we may thus inspect a constant-volume cut through the three-dimensional phase diagram.

The $z - \Delta a$ phase diagram resulting from such a cut at $v = 0.95$ is shown in Fig. 4, *A* and *B*. It includes information about the stability of stationary shapes at $q \to \infty$. Testing the stability for $q \to \infty$ is useful because switching to more realistic, finite values of q merely adds the degree of freedom to adjust Δa for the same stationary shapes (cf. Heinrich et al., 1993). Thus, shapes that are unstable at $q \to \infty$ cannot be stable at finite q, and so they need not concern us any further. In contrast, the stable stationary shapes of Fig. 4 may become unstable with respect to Δa changes, and so their stability has to be checked anew at every finite value of q.

Lines P and E in Fig. 4 were obtained for $f = 0$ and comprise the well-known prolate axisymmetric shapes of free vesicles with equatorial mirror symmetry (line P) and without such symmetry (line E), respectively. At low Δa, the mirror symmetric shapes are stable (steep, solid part of P on the left), whereas, at point S, the mirror symmetry of

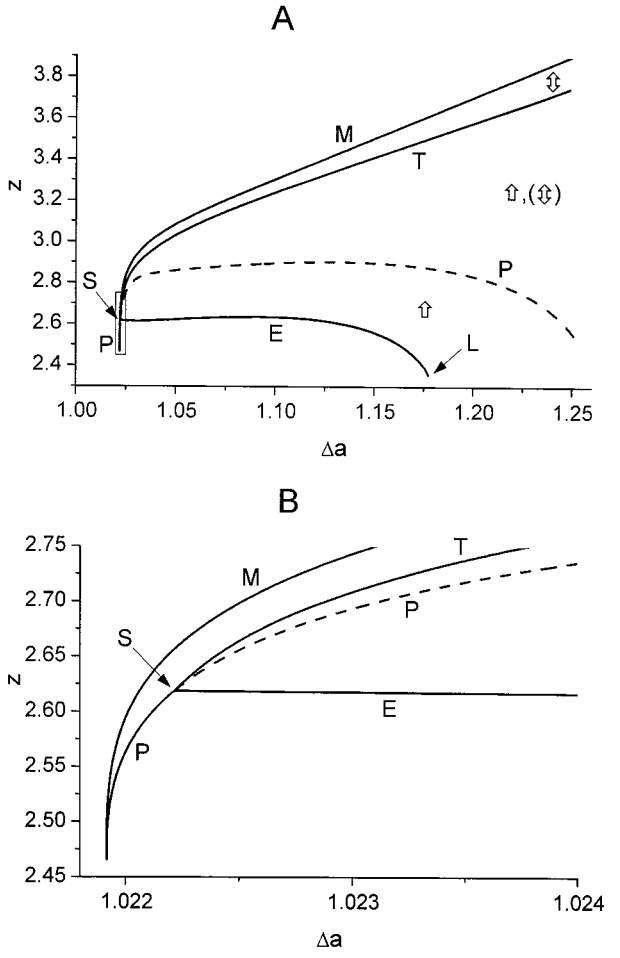

FIGURE 4 The $z - \Delta a$ phase diagram of stationary shapes of axially strained, prolate axisymmetric vesicles with relative volume $v = 0.95$ and $q \to \infty$. The rectangular inset of part (*A*) is enlarged in part (*B*). The lower two lines comprise stationary shapes of free vesicles ($f = 0$) with equatorial mirror symmetry (line P) and without such symmetry (pears, line E), respectively. The pear line (E) branches off line P at the symmetry breaking point S and ends at the limiting shape L. Elongated shapes ($f > 0$) of either symmetry are found above the respective $f = 0$ lines. In (*A*), the shape symmetries in different regions are indicated using hollow vertical arrows. The region of elongated pear shapes (*hollow up arrow*) is bounded by lines E and T, whereas elongated mirror symmetric shapes (*hollow double arrow*) are located between lines P and M. Line M marks the shapes with the largest possible pole-to-pole distance at given Δa ($f \to \infty$). The mirror symmetric shapes between the dashed part of P and line T are unstable at $q \to \infty$, which is indicated by placing the corresponding vertical arrow in parentheses. See Fig. 5 for an illustration of typical shapes along a vertical scan through this phase diagram.

stable shapes is broken. The dashed part of line P starting in S continues the sequence of now unstable mirror symmetric $f = 0$ shapes. The stable shapes beyond this point are pears (line E), with the limiting shape (point L) consisting of two different spheres connected through an infinitesimal neck. (Note that here and in the following we use "pear" to denote any prolate axisymmetric shape that is polar, i.e., that does not have an equatorial reflection plane.) For $q \to \infty$, the shape transition at S resembles a second-order phase transition that was described in Svetina and Žekš (1990).

Because we are only interested in elongated ($f \geq 0$) axially strained vesicles, we need to inspect only the shapes located above the $f = 0$ lines. The upper boundary of the region of interest ($f \to \infty$, line M) comprises the shapes with the largest possible axial extension at given Δa. It was shown (Božič et al., 1997) that these limiting shapes are mirror symmetric. Hence, there has to be a transition between mirror symmetric elongated shapes and elongated shapes with broken mirror symmetry. This transition takes place at the z values forming line T. The mirror symmetric shapes located between this line and line M are the only relevant (low-energy) solutions of the considered variational problem in this region. Alternately, at every point between line T and line P one finds two relevant solutions, i.e., a mirror symmetric stationary shape and a stationary shape with broken mirror symmetry. In this case, the mirror symmetric shape is unstable. This situation is illustrated in Fig. 5 showing a vertical scan through the $z - \Delta a$ phase diagram at $\Delta a = 1.1$. It presents the local bending energies of both solutions as a function of z and includes a few typical shapes.

Shape sequences and force–extension relations at $q = 4$

Having mapped the stationary shapes into the above phase diagram, we need to establish which of these shapes are successively assumed by a real axially strained vesicle. Thus, we now consider more realistic, finite values of the ratio q between the nonlocal and the local bending modulus. Measured values of the nonlocal bending modulus k_r agree with estimates considering the membrane as a double layer of two homogeneous thin shells (Waugh et al., 1992; Raphael and Waugh, 1996), both giving a value for k_r that is three to four times the value of the local bending modulus k_c. We choose $q = 4$ as a typical ratio. As explained above, within this generalized bilayer couple model the area difference Δa is a mere geometrical quantity whose value changes as the shape of a given vesicle is deformed. In contrast, we recall that the reference value Δa_0 represents the difference between the numbers of lipids constituting the two leaflets of the bilayer membrane. Not allowing for lipid transbilayer movement (flip-flop), Δa_0 remains constant when an axial force deforms the observed vesicle, and so it is this quantity that is a basic control parameter characterizing a given vesicle.

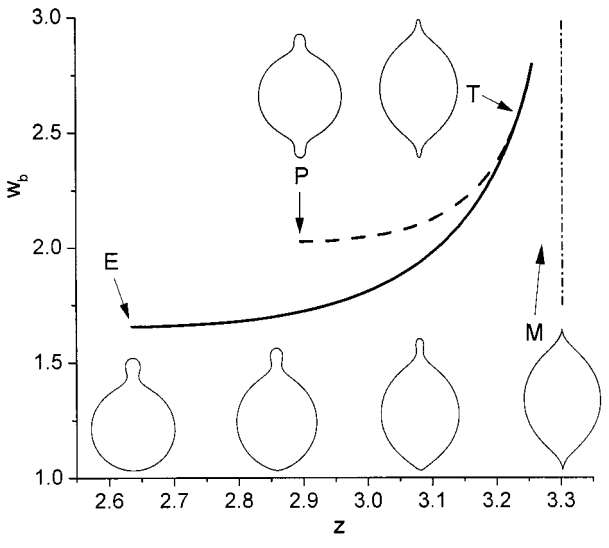

FIGURE 5 Relative local bending energy w_b of stationary shapes at $v = 0.95$ and $\Delta a = 1.1$ as a function of the dimensionless pole-to-pole distance z. A few typical shapes are included. Except for the shape at point T, they have been arranged in such a way that the position of the (vertical) symmetry axis of each shape corresponds to the z-value of this shape. Characteristic points were labeled according to the labeling of lines in Fig. 4. The energy of stable (at $q \to \infty$) shapes is depicted by the solid line starting in point E and ending (not shown) at the z-value corresponding to point M (marked by the vertical dash-point line). At low vesicle extensions, these stable shapes are nonmirror symmetric pears, whereas at point T they gain an equatorial mirror symmetry. The dashed line connecting P and T denotes the energy of unstable mirror symmetric shapes. The shapes at E and P are shapes of free vesicles ($f = 0$), whereas the limiting shape at M corresponds to an infinitely large axial force.

Before turning to the shape behavior of axially strained vesicles, it is useful to recall a well-known result of the study of free vesicles. Comparing the stable prolate shapes obtained for $q = 4$ at continuously increasing values of Δa_0 reveals a large jump between mirror symmetric vesicle shapes and pear shapes having an almost closed neck (Svetina and Žekš, 1992; Miao et al., 1994). This discontinuous (first-order) transition is accompanied by a discontinuous change of Δa at the critical value of Δa_0. The intermediate Δa-values correspond to unstable or metastable stationary shapes. Hence, a number of stationary shapes of free vesicles that are stable at $q \to \infty$ become indeed globally unstable when they gain the freedom to adjust Δa.

We are, of course, mainly interested in the behavior of those stationary $f = 0$ solutions that correspond to globally stable shapes, i.e., to real free vesicles. When subjecting these vesicles to an axial strain, we observe a surprising and highly interesting variety of shape transformations. The particular shape sequence of a strained, elongating vesicle mainly depends on the vesicle's Δa_0 value. Furthermore, a given vesicle may behave differently in the two considered experimental scenarios (constant-z or constant-f scenario, cf. Fig. 3). Figure 6 presents an overview of the different types of behavior observed. It combines three typical shape sequences obtained for representative axially strained, prolate vesicles. The first two example vesicles (A: $\Delta a_0 = \Delta a|_{f=0} \approx 1.02209$; and B: $\Delta a_0 = 1.7$, $\Delta a|_{f=0} \approx 1.02214$) are mirror symmetric at $f = 0$. As the vesicle extension increases, the mirror symmetry is broken in both cases. In the constant-z scenario the symmetry-breaking transition takes place along the path marked J_z. This transition is continuous for vesicle A, whereas it is discontinuous for vesicle B. Alternately, in the constant-f scenario, the symmetry-breaking transition (along path J_f) is discontinuous for both vesicles. The shapes of the third example vesicle (C: $\Delta a_0 = 1.9$, $\Delta a|_{f=0} \approx 1.17624$) are nonmirror symmetric throughout the depicted series, and all shape changes are continuous.

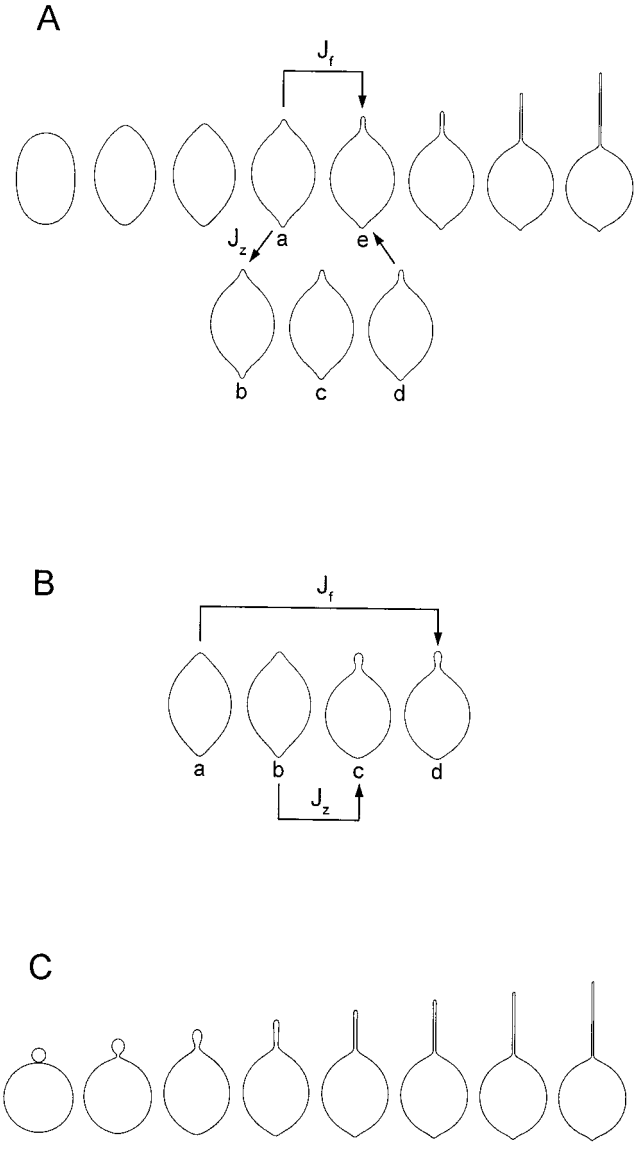

FIGURE 6 Shape series of three axially strained example vesicles chosen at increasing Δa_0 values: (*A*) $\Delta a_0 = 1.02209$, (*B*) $\Delta a_0 = 1.7$, and (*C*) $\Delta a_0 = 1.9$. For all vesicles, $v = 0.95$ and $q = 4$. The shape series A and C both start with the shape of the free vesicle ($f = 0$). *B* shows only shapes that are immediately involved in the symmetry-breaking transition. Shapes before and after this transition (not shown) are similar to those in *A*. The shape series *A* and *B* depend on the considered scenario. Parts of shape paths that are different in the two scenarios were labeled J_f and J_z, respectively. J_f marks the symmetry-breaking transition in the constant-*f* scenario. This transition is a discontinuous jump between shapes a and e in *A* and between shapes a and d in *B*, respectively. In the constant-*z* scenario, a similar discontinuous transition occurs in *B* between shapes b and c (labeled J_z). However, the symmetry-breaking transition in *A* is continuous in the constant-*z* scenario (along path J_z). In this case, the vesicle passes smoothly through shapes a–e, changing its symmetry at b = T. In *C*, all shape changes are continuous. See also the Appendix.

Figure 6 only includes shapes that are globally stable in at least one of the two possible scenarios. The computational procedure to arrive at such shape sequences is rather lengthy. For each vesicle (i.e., for each Δa_0), one first needs to find all branches of stationary solutions that are relevant in the considered range of the axial force *f* or the pole-to-pole distance *z*. Figure 7 shows the force–extension curves of stationary solutions for the three example vesicles used in

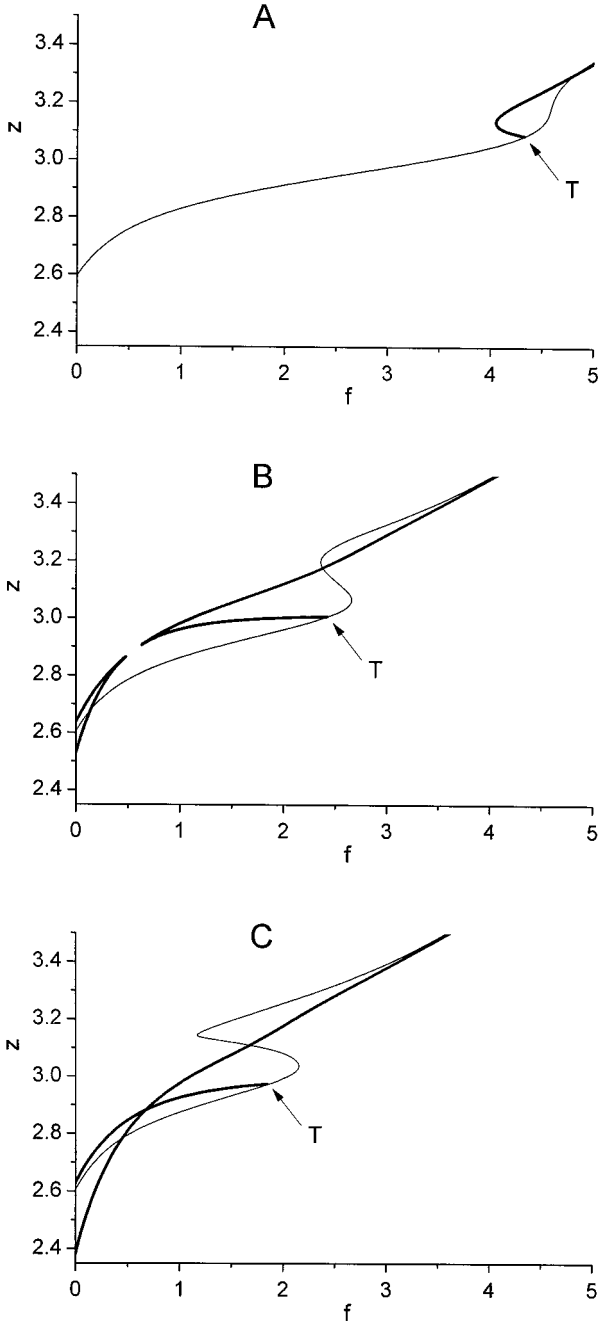

FIGURE 7 Force-extension curves for the three example vesicles shown in Fig. 6. The three parts, *A–C* are arranged in the same order as in Fig. 6, i.e., Δa_0 increases from *A* to *C*. Thin lines correspond to mirror-symmetric stationary shapes, whereas the thicker lines represent *f–z* relations of stationary pears. Points labeled T belong to line T of Fig. 4 and mark the junctions of curves corresponding to shapes with different symmetries. The *f–z* relations are continued for larger forces in Fig. 8. For a vesicle with a characteristic size $R_S = 10\ \mu$m and a membrane bending modulus $k_c = 10^{-19}$ J, one unit of the dimensionless force *f* corresponds to 0.25 pN. For more details, see the text and the Appendix.

Fig. 6. The graphs clearly demonstrate that the variety of stationary solutions is quite complex. Being able (within the Ritz method) to analyze the stability of stationary solutions proves to be extremely useful because it allows us, in a next step, to focus our attention exclusively on the locally stable shapes. Eventually, whenever two or more locally stable solutions coexist at a given value of the control parameter (f or z), the globally stable shape is obtained as the solution with the lowest total energy. The interesting but somewhat technical details of this procedure are given in the Appendix. It presents enlarged graphs of the critical regions of Fig. 7, *A* and *B* that reveal the (f, z) locations of shapes labeled by small letters in Fig. 6. Furthermore, the Appendix also visualizes the deformation of the three example vesicles by presenting the various solution branches as trajectories in the catalog of stationary shapes that was originally introduced in Fig. 4.

Let us concentrate here mainly on the more practical aspects of the force–extension relations of the three example vesicles (Figs. 7, *A–C* and 8). Fig. 8 continues the *f–z* curves of Fig. 7 for higher forces. In these graphs, we generally use thin lines to represent the *f–z* relation of axially strained, mirror symmetric stationary shapes, whereas thicker lines correspond to axially strained pear shapes. Fig. 7, *A–C* reveals how the interconnection of different solution branches evolves at increasing Δa_0. At the largest depicted forces (upper right regions of Fig. 7, *A–C* and all of Fig. 8) the globally stable solutions are, in all three cases, the pear shapes of the thick branch. (Note that, although at higher forces the thin branch of mirror symmetric shapes becomes indistinguishable from the thick pear branch, it does not merge with the latter branch but remains an independent solution.) For the third example vesicle (Fig. 7 *C*) this pear branch is globally stable at all forces down to $f = 0$. In contrast to that, the globally stable solutions of the lower-force regions of Fig. 7, *A* and *B* are the mirror symmetric shapes of the thin line (cf. also Fig. 6). The critical region of the transition between globally stable solutions of different symmetries shifts to lower forces as we increase Δa_0. For more details concerning the actual character of this transition, see the Appendix.

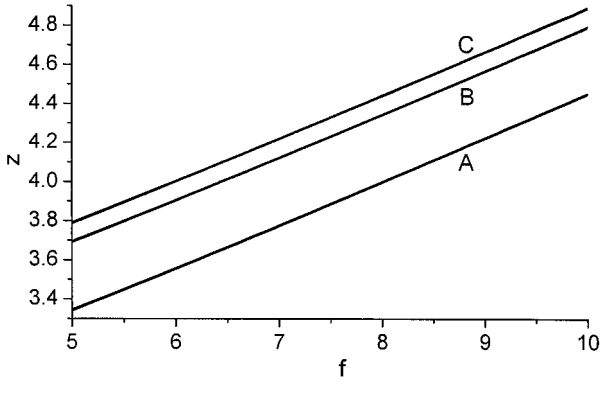

FIGURE 8 Continuation of the force–extension curves of the three example vesicles of Fig. 7 for relative forces $f \geq 5$. The curves were labeled according to parts *A–C* of Fig. 7. Note that, for each vesicle, two different lines corresponding to mirror symmetric and nonmirror symmetric shapes are shown but are indistinguishable.

It should be mentioned that new, nonmirror symmetric solutions (not shown) continue to branch off the thin line of mirror symmetric shapes as the force increases. The first of these additional branches appears at $f \approx 5.03$ (vesicle A), $f \approx 2.51$ (vesicle B), and as low as $f \approx 1.42$ for vesicle C. The corresponding transitions are in all cases continuous. As one would expect, the stability of the mirror symmetric shapes changes at this branching point, i.e., the mirror symmetric branch actually gains a weak local stability. At even larger forces, the local stability of mirror symmetric shapes alternates whenever a new nonmirror symmetric solution branch appears. Accordingly, the stability of each new, nonmirror symmetric branch is opposite from the stability of the respective mirror symmetric solution. This behavior can be easily understood and will be addressed in a later section. For now, it should only be noted that the energy of all such branches is always significantly higher than the energy of the coexisting, globally stable pear branch.

A particularly interesting result is that all three vesicles behave similarly at higher forces. The vesicles corresponding to the lines in Fig. 8 generally have a tethered shape (cf. e.g., the last three shapes in Fig. 6 *A* and *C*). The mirror symmetric shapes have shorter tethers on both sides of the main vesicle body and a reflection plane containing the equator of the main body. As mentioned above, the force–extension curves of mirror symmetric and nonmirror symmetric shapes become almost identical at larger forces. They are practically indistinguishable in Fig. 8. This applies also to the additional solution branches mentioned in the previous paragraph. Most interestingly, in the force range depicted in Fig. 8 the unified *f–z* curves become almost linear, i.e., the tethered vesicles act as almost ideal Hookean springs. The spring constant appears to be the same for all three vesicles, i.e., it becomes independent of the value of Δa_0 in this force range. This may prove very useful for practical purposes, because Δa_0 is usually hard to measure experimentally. The results of Fig. 8 suggest the system "two-point attached, tethered vesicle" as a good candidate for an ultrasensitive spring in micromechanical experiments. Alternately, the force needed to hold a vesicle at a given extension clearly depends on the value of Δa_0, i.e., on the difference between the numbers of lipids constituting the two membrane leaflets, and thus on vesicle history. The tether formation from vesicles with larger Δa_0 values requires lower forces, which is mainly due to the smaller nonlocal bending deformation accompanying tether formation from vesicles with larger Δa_0. This feature may provide a convenient way to measure Δa_0 experimentally.

In conclusion of this section, we emphasize that, beyond a certain force, the globally stable shapes (at $q = 4$) are, in all considered cases, asymmetrical. They consist of a lemon-shaped main vesicle body and a narrow membrane tether that has been pulled out of the main body. Accordingly, we

call the transitions studied above tethering transitions. Note that the tethering transition is a continuous shape change if the $f = 0$ shape of a given vesicle is already asymmetrical. Figures 7, *A–C* and 8 demonstrate that large Δa_0 values tend to favor the formation of a tether. Beyond the tethering transition, the main body of a tethered vesicle becomes more spherical at increasing pole-to-pole distances, and the tether width reduces (see Fig. 6). This agrees well with experimental observations (cf. Figs. 1 and 2).

Phase diagrams at $q = 4$

The above examples provide a basic insight into the typical shape behavior of axially strained vesicles. It is instructive to generalize the results by extending the study to the whole range of Δa_0 values of prolate vesicles. Repeating the calculations of the previous section for a large number of vesicles, we have mapped the resulting globally stable shapes into comprehensive $q = 4$ phase diagrams. The natural choice of control parameters for such diagrams is $(\Delta a_0, f)$ in the constant-f scenario and $(\Delta a_0, z)$ in the constant-z scenario. The respective phase diagrams are shown in Fig. 9, *A* and *B*.

In both diagrams, a given vesicle is mapped to its Δa_0 value on the *x*-axis, whereas the vesicle's deformation due to axial strain is reflected by a vertical upward movement in either figure. The depicted Δa_0 range roughly corresponds to globally stable, prolate vesicle shapes. The thick lines (G_f in Fig. 9 *A*, and G_z in Fig. 9 *B*) divide the region of strained vesicles into subregions of mirror and nonmirror symmetric shapes, respectively. The globally stable mirror symmetric shapes are confined to the lower left regions of both figures. The diagrams confirm that at increasing deformation the globally stable shape of every prolate vesicle will eventually be nonmirror symmetric.

Note that the global stability lines, G_f and G_z, generally mark different shape transitions in Fig. 9, *A* and *B* (cf. the paths labeled J_f and J_z in Fig. 6, *A* and *B*). In the constant-f scenario (Fig. 9 *A*), the transition across line G_f is everywhere discontinuous. Alternately, line G_z in Fig. 9 *B* consists of two distinct parts. To the left of the critical point C_z, line G_z is identical with line T, marking a continuous symmetry-breaking transition between mirror symmetric and non-mirror symmetric globally stable shapes. To the right of point C_z, the transition at line G_z is discontinuous. In this region, line T (*dash-dot line*) merely marks the locations where globally unstable branches of different symmetries merge. It should briefly be mentioned that, in both scenarios, there is a small range of Δa_0 values where a deforming vesicle crosses the respective G line twice. In this range, the $f = 0$ shapes are pears. At increasing deformation, they reach a small range of intermediate forces where their energy becomes larger than the energy of the coexisting mirror symmetric shapes. Passing the respective G line for the second time, the pear shapes become globally stable again.

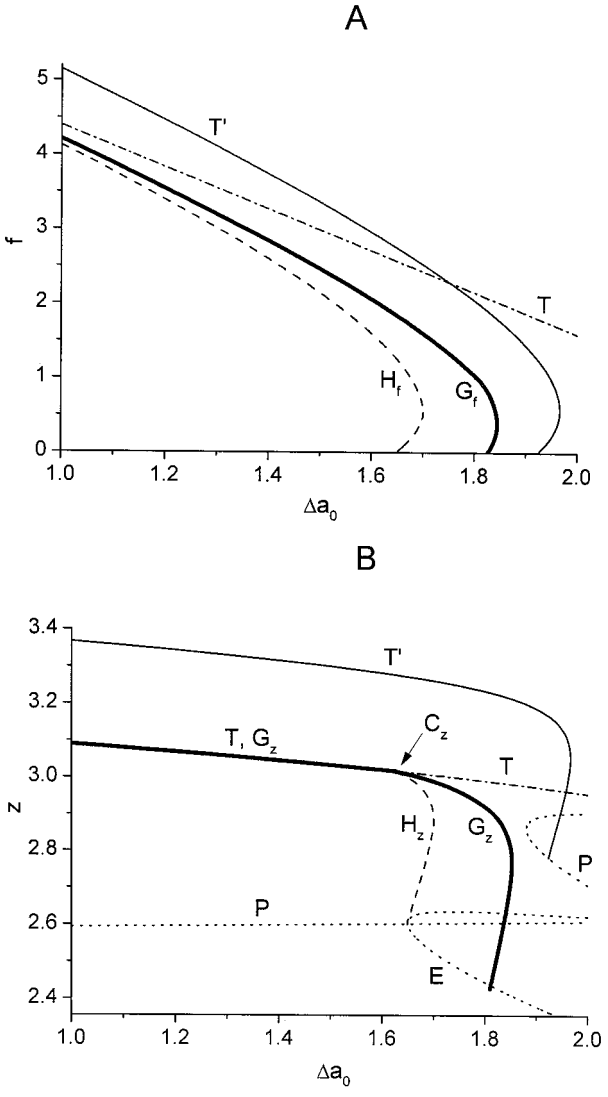

FIGURE 9 Phase diagrams of axially strained, prolate vesicles in the two scenarios at $q = 4$ ($v = 0.95$). (*A*) $\Delta a_0 - f$ phase diagram for the constant-f scenario; and (*B*) $\Delta a_0 - z$ phase diagram for the constant-z scenario. The G-lines (G_f in *A* and G_z in *B*; *thick, solid lines*) separate the region of globally stable mirror symmetric shapes (left of the respective G-line) from the region of globally stable pear shapes. The H-lines (H_f in *A* and H_z in *B*; *dashed lines*) mark the locations where stationary pear shapes first appear at increasing Δa_0. Lines T (*dash-dot*) and T′ mark junctions between branches of stationary shapes with different symmetries. Point C_z (in *B* only) is a critical point at which the character of the shape transition across line G_z changes. To the left of C_z, this transition (at line T = G_z) is continuous, whereas it is discontinuous to the right of C_z. The dotted lines P and E (in *B* only) are the lines of stationary shapes of free vesicles ($f = 0$).

In the previous section, we have mentioned that additional nonmirror symmetric solutions continue to appear at increasing deformation. Fig. 9, *A* and *B* include a line T′ that marks the locations at which the first of these new solution branches appears in the depicted Δa_0 range. For further illustration, we have also included the (*dashed*) lines H_f and H_z. These lines subdivide the region of globally stable mirror symmetric shapes into a part where mirror

symmetric shapes are the only stationary solution (left of the respective H line) and a part that additionally contains globally unstable pear shapes. Furthermore, the dotted lines P and E of stationary $f = 0$ solutions were included in Fig. 9 *B* to illustrate the locations at which various other lines originate. The lower branches of lines P and E also represent the lower boundary of this phase diagram.

Tether shape and degeneracy of tethered vesicles

Already, in the discussion of Figs. 7 and 8, we have noted that the force–extension curves of mirror symmetric and nonmirror symmetric shapes become almost identical at larger forces. Each of the *f–z* lines of the three example vesicles (A–C) shown in Fig. 8 actually represents a set of various distinct solutions, including the additional nonmirror symmetric solutions that successively appear at increasing deformation (e.g., at line T′, cf. Fig. 9). Both the shapes of the latter nonmirror symmetric solutions as well as the mirror symmetric shapes have tethers on both sides of the main vesicle body. The near-identity of the *f–z* curves of different stationary solutions of a given vesicle strongly indicates that the tether is basically cylindrical. Obviously, we may cut off the tether on one side of the mirror symmetric shape and attach it to the tether on the other side without significantly affecting the axial force. If the tether were not cylindrical but, for example, an elongated cone, we could not do this manipulation without deforming some parts of the vesicle, which, in turn, would hardly be possible without a force change. Alternately, we found that, in all considered cases, the globally stable asymmetrical shape has a significantly lower energy than the other solutions. Furthermore, the stability analysis reveals a pronounced minimum for the globally stable asymmetrical solution, whereas the mirror symmetric solution and the additional nonmirror symmetric solutions are more or less degenerate with respect to one degree of freedom.

To resolve this puzzle, we have simulated a situation where we can push the main vesicle body along the tether while the pole-to-pole distance remains constant. This was done by introducing another constraint that enforces a fixed distance z_m between the lower pole of the vesicle and the equator of the main vesicle body. Continuously changing this distance, we have monitored the resulting shapes and their elastic energy for vesicle A at $z = 4.5$. Energy and shapes are combined in Fig. 10. Inspecting the z_m dependence of the elastic energy explains at once the degeneracy of the mirror symmetric shape and all other shapes involving two tethers. We see that we may indeed cut out a (more or less) cylindrical part of the tether on one side and add it to the tether on the other side without changing the elastic energy as long as at least a small tethered part remains on either side of the main vesicle body. Only when the tether completely disappears on one side the vesicle slides down into the energy minimum of the globally stable, asymmetrical shape. Of course, there have to be two equivalent energy minima because flipping a given shape vertically does not affect its energy. The energy difference between the minimum and the broad plateau of vesicles with two tethers can thus be ascribed to the high energy that is needed to initialize a tether, i.e., to bend the membrane into a tether right at the pole. This energy cost is paid only once if the vesicle has only one tether, which explains the global stability of the corresponding asymmetrical shape.

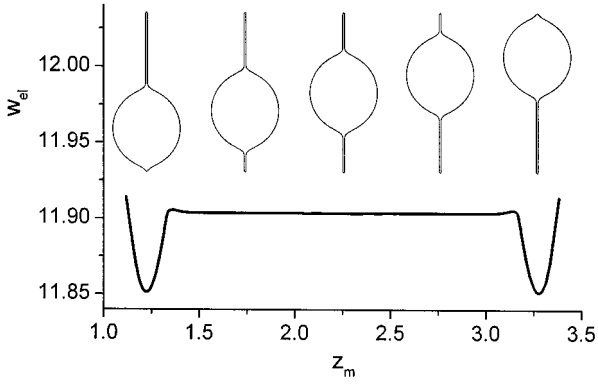

FIGURE 10 Relative elastic energy and typical shapes of a vesicle (vesicle *A* of Fig. 6 at $z = 4.5$) whose main body is pushed along the tether, as a function of the distance z_m of the equator of the main body from the lower vesicle pole. The vertical symmetry axis of each shape has been aligned corresponding to the value of z_m. The central energy plateau is practically flat, but close inspection reveals small deviations from an ideal straight line. These deviations are more pronounced toward the plateau edge. The deep energy minimum corresponds to a shape with a single tether on one of its sides. For $k_c = 10^{-19}$ J, the energy difference between the minimum and the plateau is $\approx 30\, k_B T$.

These results further support that the tether shape is practically cylindrical. In contrast, if we require smoothness of the higher derivatives of the vesicle contour, it is rather unlikely that the tether is an ideal cylinder. Another indication for the existence of (small) deviations from a cylindrical tether shape is the observation that the energy plateau in Fig. 10 is not ideally flat. A small but significant energy maximum is seen adjacent to the minimum of the globally stable shape. It corresponds to that additional nonmirror symmetric stationary solution that appears first at increasing deformation (at line T′ in Fig. 9). Of course, the energy plateau of Fig. 10 exhibits further minima or maxima for all other additional solutions. However, they are too weak to be recognized.

The presence of the noticeable first maximum suggests that the deviations of the tether shape from a cylinder are largest at the vesicle pole and/or the junction with the main vesicle body. To establish the importance of such deviations, we have recalculated the globally stable shape of vesicle A at $z = 4.5$ with very high accuracy. For this, the number of terms included in the shape expansion of the Ritz method was doubled to 200. The resulting tether shape is enlarged in Fig. 11, where the tether is somewhat distorted by the scales used for the coordinate axes. This microscopic picture of the tether contour confirms that, over most of its

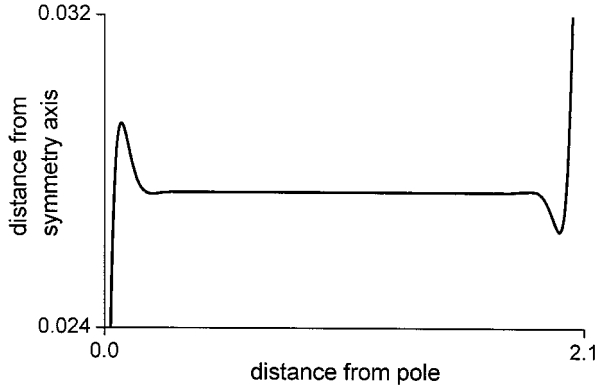

FIGURE 11 Microscopic picture of the tether of vesicle *A* of Fig. 6 (at $z = 4.5$) as calculated by the Ritz method with a very high accuracy. Only one side of the tether contour is shown, with the vesicle's symmetry axis oriented horizontally. Note that the scales were chosen to maximally enhance the shape of the tether contour. Apart from perturbations at the vesicle pole (on the left) and at the junction with the main vesicle body (on the right), the tether is practically cylindrical.

length, the tether is indeed indistinguishable from a cylinder. As indicated in Fig. 10 by the dependence of the elastic energy on z_m, significant deviations of the tether shape from an ideal cylinder are found only at the pole and at the junction with the main body. Recent analytical results prove that these deviations act as perturbations superposing a wave-like shape with a fast decaying amplitude on the mean, cylindrical tether shape. (The details of this analysis will be published elsewhere.) For most practical purposes, however, these waves do not significantly alter the underlying cylindrical shape of the tether.

CONCLUSIONS

The present theoretical paper studies the shape behavior of bilayer vesicles that are deformed by axial loads acting on two opposite points of the vesicle membrane. Restricting the calculations to prolate axisymmetric vesicle shapes, the use of general variational procedures allows us to consider arbitrary deformations and thus to overcome the limitations of parametrical models. To cover a large range of deformations, we employ or introduce mathematical methods that are particularly suitable for the description of axially strained vesicles.

Vesicles subject to low axial forces are shown to exhibit a highly interesting and rather complex variety of elongated shapes. With the exception of the work by Umeda et al. (1998), previous studies of axially strained vesicles have been restricted exclusively to mirror symmetric shapes (Božič et al., 1997; Kuchnir Fygenson et al., 1997b, where the latter work's simplifications in the physical description of closed bilayer membranes, as well as in the parametrical treatment, may have led to substantial uncertainties in the quantitative predictions made). Although some of the conclusions drawn in the very recent paper by Umeda et al. (1998) are in agreement with our results, that paper disregards the nonlocal bending deformation, and it also allows the vesicle volume to change (keeping the pressure difference across the membrane constant). It should be mentioned that, for the deformations considered here, mechanically induced pressure differences across the membrane are negligibly small in comparison with pressures generated by osmotic imbalance. Therefore, because the vesicle membrane is practically impermeable to osmotically active substances over the time frame of an experiment, the vesicle volume cannot change as long as the external conditions (temperature, osmolarity) are kept constant.

The various phase diagrams (Figs. 4 and 9) presented here for prolate vesicles with a relative volume $v = 0.95$ include shapes with and without equatorial mirror symmetry. Fig. 4 gives a representative overview of the stationary shapes of axially strained vesicles within the generalized bilayer couple model. For a characteristic ratio, $q = 4$, between the nonlocal and the local bending modulus, Fig. 9 reveals the regions of globally stable shapes of different symmetries in dependence of the vesicle's area difference of monolayers, Δa_0, and its axial deformation. On this basis, we find that only a small fraction of the mirror symmetric shapes studied earlier correspond to stable solutions of the considered variational problem. Generally, the shape behavior of axially strained vesicles is shown to be dominated by polar shapes, i.e., by shapes with broken mirror symmetry. For $q = 4$, we inspect the detailed shape behavior of typical model vesicles, and we demonstrate how additional instabilities may occur.

Higher forces are found to cause the formation of narrow tubular membrane extrusions. This tethering transition may be continuous or discontinuous. Its character depends on how the vesicle elongation is controlled (i.e., whether an increasing axial force or an increasing pole-to-pole distance is imposed), and on vesicle history (i.e., on the difference between the numbers of lipids constituting the two membrane leaflets, which is basically established when a vesicle forms). Starting from free vesicles with prolate shapes, we find that elongation of any such vesicle will eventually lead to an asymmetrical shape. Although shapes involving tethers on both sides of the lemon-shaped main vesicle body may exist in a metastable or locally degenerate state for a considerable time, the ultimate, globally stable shape of a tethered vesicle always consists of the main vesicle body and a single tether on one of its sides. (We cannot exclude that vesicles having smaller Δa_0 values than the prolate vesicles studied here may initially form tethers on both poles in a symmetrical fashion. However, we expect that, also in this case, there is a critical vesicle extension at which the asymmetrical shape becomes globally stable.) Finally, inspecting the microscopic shape of the tether, we demonstrate that, for most practical purposes, it is safe to describe the tether by a cylinder.

We emphasize that the numerical results presented here were based on the currently accepted model for the appropriate description of the shapes of lipid bilayers. This generalized bilayer couple model has proven to be a powerful

and reasonably accurate model that has satisfactorily reproduced a number of experimental observations made on free phospholipid vesicles. The present work extends this model by including the effect of an axial load. Our results indicate that, in most cases, omission of any part of this framework (like, e.g., disregard of the nonlocal bending energy or an inappropriate treatment of the two constraints of membrane area and vesicle volume) will result in a poor theoretical description of related experiments.

The results of the present study provide the basis for a better understanding of a variety of experiments including preliminary observations reported here for the first time. For example, we are able to explain the formation of membrane tethers, which, in a number of experiments, have been used to establish important mechanical characteristics of artificial and biological membranes. Furthermore, the physical situation that we describe theoretically reflects two quite different and yet, as far as membrane mechanics are concerned, practically equivalent experiments. In the first type, the vesicle is fixed at one point while a pulling force acting on a different point of the vesicle membrane causes the deformation studied above. A prototype of this experiment is documented in Figs. 1 and 2. The observed vesicle shapes are in a striking qualitative agreement with our theoretical results. In addition, the present analysis applies equally well to a second kind of experiments in which a rod-like structure growing inside a vesicle pushes two points of the vesicle membrane apart. In recent experiments of this type (Hotani and Miyamoto, 1990; Kuchnir Fygenson et al., 1997a, b; Umeda et al. 1998), the pushing force was exerted by microtubules that assembled spontaneously inside phospholipid vesicles. The resulting shapes are again in general agreement with our predictions.

Although the results included in this study appear to represent the principal shape behavior of axially strained vesicles quite comprehensively, the present work is far from providing a complete picture of the manifold of possible shapes. To avoid overburdening of this paper, we have considered only vesicles with a relative volume of 0.95, and we have kept the ratio between the nonlocal and the local bending modulus fixed at $q = 4$. Thus, instead of documenting extensive studies of the effects of changes in these parameters, we have chosen to present the tools that enable us to perform such studies and to demonstrate their application to a few representative examples. The analysis of further details seems more instructive and manageable only when carried out as part of the interpretation of specific experimental data. Because it is feasible that experimental results including accurate measurements of the relative vesicle volume and of the force–extension relation will soon be available, we hope to be able to apply the theoretical framework developed here to concrete practical observations in the near future. This will certainly provide another way to verify the validity of the generalized bilayer couple model, and it may also enable us to deduce additional information about the mechanical properties of bilayer membranes.

APPENDIX

In the main text we have given an overview of the different types of possible shape transitions of axially strained vesicles. Let us provide here a more detailed illustration of the interesting and, in some aspects unusual, properties of this physical system.

Figure 12 enlarges the critical region of the force–extension graph (Fig. 7 *A*) of the first example vesicle. As before, thin lines represent mirror symmetric shapes. For this vesicle, the pear shapes of the thick branch are the first nonmirror symmetric stationary solutions found for $f \geq 0$ at increasing deformation, i.e., for lower forces, the mirror symmetric branch is the only stationary solution. As therefore expected, the mirror symmetric shapes are locally stable up to point T in both considered scenarios (constant-*z* and constant-*f*). Beyond point T, the mirror symmetric branch is found to be unstable in both scenarios. In the constant-*z* scenario, the mirror symmetric branch remains the only solution up to point T. Thus, the corresponding mirror symmetric shapes must also be globally stable. The symmetry-breaking transition at point T is a typical second-order transition in this scenario. The new pear branch is locally stable and, because it is the only locally stable stationary solution above point T, it is also globally stable. Therefore, at increasing pole-to-pole distance, the vesicle smoothly changes its symmetry, assuming the shapes a, b, c, d and e (cf. Fig. 6 *A*, path J_z) in a continuous manner. The situation is quite different in the constant-*f* scenario. In this case, there are three stationary solutions in the force range between points d and b (=T). The part of the pear branch above point d is found to be locally stable, whereas the strained pear shapes between points b and d are unstable. The latter shapes correspond to a maximum of the total energy, representing the energy barrier between the two locally stable shape branches of different symmetries that coexist in this force range. Plotting the energy as a function of the force (Fig. 13) reveals the critical force $f_{crit} \approx 4.14$ at which the global energy minimum shifts from mirror symmetric to nonmirror symmetric shapes. This discontinuous, first-order transition is marked in Fig. 12 by the vertical dashed line (J_f) connecting points a and e. In this case, we expect the vesicle shape to jump from shape a to shape e when the force reaches the critical value f_{crit} (cf. Fig. 6 *A*, path J_f).

The *f*–*z* graph of the second example vesicle (Fig. 7 *B*) shows an additional low-force pear branch. However, at low forces the globally stable shapes are still mirror symmetric, i.e., the shapes of the lower pear branch of Fig. 7 *B* are unstable or metastable and are not assumed by the vesicle. Inspection of the critical region (enlarged in Fig. 14) reveals a behavior that is even more complex than that of the first vesicle and involves discontinuous transitions in both scenarios. As before, the abrupt

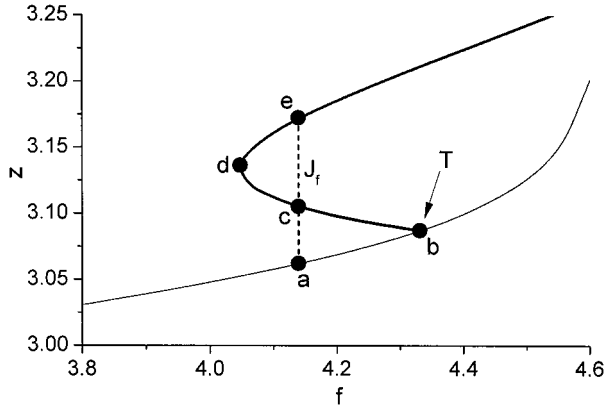

FIGURE 12 Enlarged critical region of the force–extension relation of the first example vesicle (Fig. 7 *A*). The shapes corresponding to points a–e are shown in Fig. 6 *A*. At increasing pole-to-pole distance (constant-*z* scenario), the vesicle undergoes a continuous (second-order) symmetry-breaking shape transition at point T. Alternately, at increasing force (constant-*f* scenario) a discontinuous (first-order) transition occurs between points a and e (*vertical dashed line* J_f, cf. also Fig. 13).

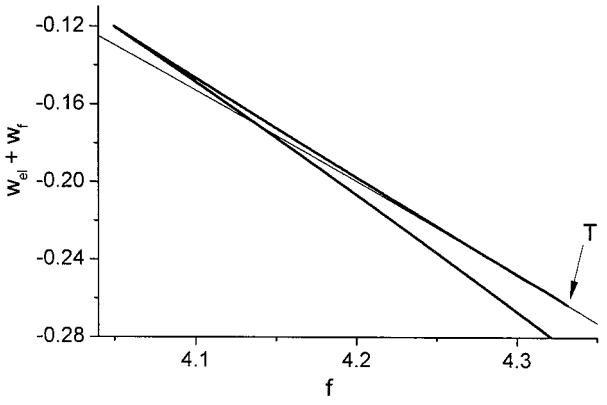

FIGURE 13 Relative total energy as a function of the dimensionless force for the first example vesicle (Figs. 12 and 7 *A*) in the constant-*f* scenario. As before, the thin line corresponds to mirror-symmetric stationary shapes, and T marks the junction with the thicker line showing the energy of pear shapes. A first-order transition at $f_{crit} \approx 4.14$ shifts the minimum-energy state from mirror symmetric shapes to asymmetrical shapes.

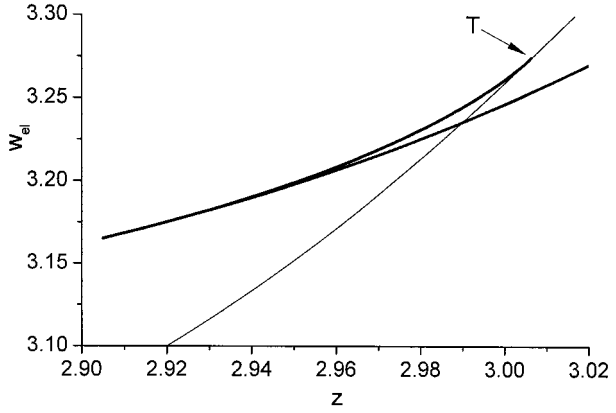

FIGURE 15 Relative elastic energy as a function of the dimensionless pole-to-pole distance for the second example vesicle (Figs. 14 and 7 *B*) in the constant-*z* scenario. A discontinuous (first-order) transition occurs between mirror symmetric shapes (*thin line*) and nonmirror symmetric shapes (*lower thick line*) at $z_{crit} \approx 2.99$.

shape change in the constant-force scenario (a → d) is marked by a vertical dashed line (J_f, $f_{crit} \approx 1.61$). A similar jump occurs now also in the constant-*z* scenario. Unlike in Fig. 12, the pear branch now has a positive slope at point T, making a continuous symmetry-breaking transition impossible. Moreover, the part of the pear branch between point T and the sharp kink (to the left in Fig. 14) is found to be unstable. The dependence of the elastic energy on the pole-to-pole distance (Fig. 15) shows a first-order transition ($z_{crit} \approx 2.99$). This transition is marked in Fig. 14 by the horizontal dashed line J_z connecting points b and c. The shapes that are immediately involved in these transitions are shown in Fig. 6 *B*, where the two discontinuous shape changes are labeled using the same notation as in Fig. 14.

Compared to the first two example vesicles, the behavior of the third is trivial (cf. Figs. 6 *C* and 7 *C*). In both scenarios, it simply follows the thick line (Fig. 7 *C*) that is characterized by the smallest pole-to-pole distance at $f = 0$. In this case, all globally stable shapes are asymmetrical, and the shape changes are everywhere continuous.

Let us finally return to Fig. 4 and present yet another, useful view at our numerical results. As "$q \to \infty$ phase diagram," Fig. 4 contains only a limited amount of information regarding the globally stable shapes of real vesicles, i.e., of vesicles with finite q values. However, as a catalog of stationary shapes, this figure is quite useful, because it maps all principally possible stationary shapes (at $v = 0.95$) into a single diagram. Moreover, with Δa and z as geometrical control parameters, this mapping is done in a continuous fashion, i.e., adjacent locations in Fig. 4 are generally occupied by similar shapes. To use Fig. 4 to visualize the behavior of a vesicle with finite q, one simply has to connect the locations of stationary shapes that are successively assumed by this vesicle.

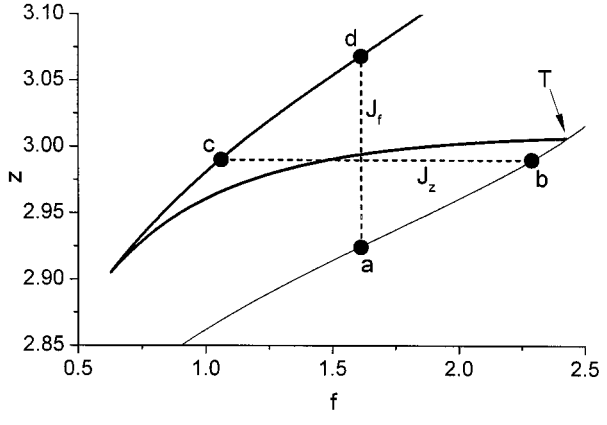

FIGURE 14 The critical region of the force–extension relation of the second example vesicle (Fig. 7 *B*) is enlarged. The shapes corresponding to points a–d are shown in Fig. 6 *B*. Discontinuous symmetry-breaking shape transitions occur in both scenarios. They were marked by the dashed lines J_z (constant-*z* scenario, cf. also Fig. 15) and J_f (constant-*f* scenario).

This is demonstrated in Fig. 16. For clarity, we have omitted most of the lines included originally in Fig. 4, keeping only the solid $f = 0$ branches E and P. In addition, a few points belonging to line T have been marked. New lines are the stability lines G_f (*solid, thick*) and H_f (*dashed*, cf. Fig. 9 *A*). Considering here only the constant-*f* scenario, these lines add the information about the stability of stationary shapes at $q = 4$ to the shape catalog. Note that line G_f consists of two parts that meet, along with line H_f, in a single point belonging to line T. Below this point, line T runs to the right of the near, left part of line G_f. This left branch of line G_f comprises those mirror symmetric shapes that are obtained at the J_f transition of different vesicles (cf. points a in Figs. 12 and 14), whereas the right branch is formed by the respective pear shapes (cf. point e in Fig. 12 and point d in Fig. 14). Thus, the two branches of line G_f and line E enclose the region of globally unstable shapes. This region includes metastable mirror symmetric shapes (between the left part of line G_f and line T, e.g., the shapes between points a and T in Figs. 12 and 14), locally unstable pear shapes (between line T and line H_f, e.g., the shapes between points b and d in Fig. 12) as well as metastable stationary pear shapes (to the right of H_f, e.g., the shapes between points d and e in Fig. 12). It is seen that most stationary shapes of the $q \to \infty$ phase diagram (Fig. 4) are not assumed by a vesicle having $q = 4$.

The thin lines A, B, and C included in Fig. 16 are the trajectories of shape changes of the three example vesicles (cf. Fig. 7 *A–C*). (Note that the mirror symmetric branches are shown only up to points T.) The upper right region of Fig. 16 corresponds to nonmirror symmetric shapes that are strained by large forces and are in a tethered configuration. Here, we find the trajectories of globally stable shapes of all three vesicles. Although their $f = 0$ shapes are quite different, the three vesicles have similar shapes in this high-force range (cf. Fig. 6). Backtracking along the trajectories shows that vesicle C always remains in the region of globally stable shapes until the shape of the free vesicle ($f = 0$) on line E is reached. An independent C branch corresponds to the two low-force branches in Fig. 7 *C* that merge at T. It comprises unstable mirror symmetric shapes (left of T in Fig. 16) and unstable elongated pears (right of T). Backtracking along the trajectories A and B reveals how both run through the regions of

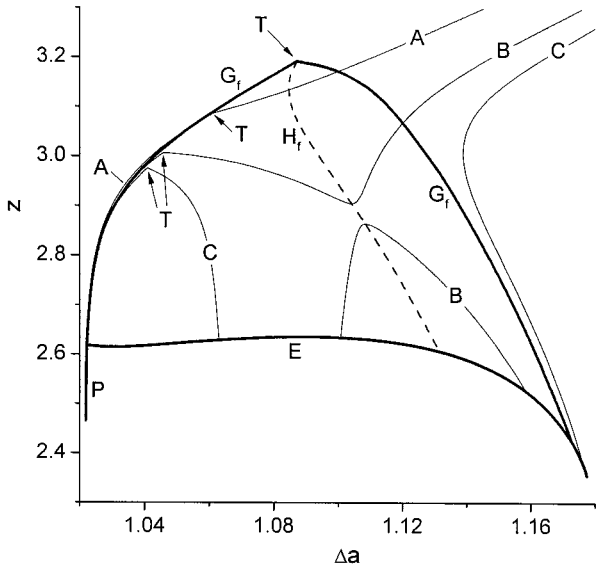

FIGURE 16 The $z - \Delta a$ phase diagram of Fig. 4 is extended by including the information about the stability of stationary shapes as established for $q = 4$ in the constant-f scenario. For the meaning of lines P, E, and T (the latter is not shown, instead, a few points of the T-line are marked), see Fig. 4. To the right of line T, the shape behavior of mirror symmetric shapes, which are globally unstable in this region, was not monitored. Shapes located above line G_f are globally stable, whereas the region enclosed by lines G_f and E comprises globally unstable shapes. The latter region is subdivided by the dashed line H_f separating locally unstable pear shapes (to the left of line H_f) from metastable pear shapes (to the right of line H_f). Trajectories (*thin lines*) of stationary shapes of the three example vesicles of Fig. 7 are included. They are labeled according to parts *A–C* of Fig. 7. Note that trajectory A and the upper part of trajectory B both originate from the left, steep part of line P. For further details see the text.

metastable and unstable shapes, until, at low forces, they cross the left branch of line G_f and become globally stable again. In both cases, the low-force globally stable shapes are mirror symmetric and originate from line P. The change of symmetry occurs at points T. The lower pear branch of Fig. 7 *B* is an independent branch in Fig. 16 (labeled also B) where it comprises unstable and metastable pear shapes. The discontinuous shape transitions of vesicles A and B in the constant force scenario thus occur between the crossings of either trajectory with the two branches of line G_f.

The experiments documented in Figs. 1 and 2 were performed by V.H. in the laboratory of R. E. Waugh, University of Rochester. We are grateful to R. E. Waugh for his permission to include the previously unpublished videographs in this paper, as well as for his critical reading of this manuscript. We also thank E. Evans for fruitful discussions, and D. Kuchnir Fygenson for sending us a paper prior to publication. This work was funded by The Ministry of Science and Technology of the Republic of Slovenia Grant No. J3-7033-381.

REFERENCES

Bo, L., and R. E. Waugh. 1989. Determination of bilayer membrane bending stiffness by tether formation from giant, thin-walled vesicles. *Biophys. J.* 55:509–517.

Božič, B., S. Svetina, B. Žekš, and R. E. Waugh. 1992. The role of lamellar membrane structure in tether formation from bilayer vesicles. *Biophys. J.* 61:963–973.

Božič, B., S. Svetina, and B. Žekš. 1997. Theoretical analysis of the formation of membrane microtubes on axially strained vesicles. *Phys. Rev. E.* 55:5834–5842.

Bukman, D. J., J. H. Yao, and M. Wortis. 1996. Stability of cylindrical vesicles under axial tension. *Phys. Rev. E.* 54:5463–5468.

Courant, R., and D. Hilbert. 1924. Methoden der mathematischen Physik. Verlag von J. Springer, Berlin.

Dai, J., and M. P. Sheetz. 1995. Mechanical properties of neuronal growth cone membranes studied by tether formation with laser optical tweezers. *Biophys. J.* 68:988–996.

Deuling, H. J., and W. Helfrich. 1976. The curvature elasticity of fluid membranes: a catalogue of vesicle shapes. *J. Phys. (Paris).* 37: 1335–1345.

Döbereiner, H.-G., E. Evans, U. Seifert, and M. Wortis. 1995. Spinodal fluctuations of budding vesicles. *Phys. Rev. Lett.* 75:3360–3363.

Döbereiner, H.-G., E. Evans, M. Kraus, U. Seifert, and M. Wortis. 1997. Mapping vesicle shapes into the phase diagram: a comparison of experiment and theory. *Phys. Rev. E.* 55:4458–4474.

Evans, E. A. 1974. Bending resistance and chemically induced moments in membrane bilayers. *Biophys. J.* 14:923–931.

Evans, E. A. 1980. Minimum energy analysis of membrane deformation applied to pipet aspiration and surface adhesion of red blood cells. *Biophys. J.* 30:265–284.

Evans, E., and A. Yeung. 1994. Hidden dynamics in rapid changes of bilayer shape. *Chem. Phys. Lipids.* 73:39–56.

Heinrich, V., M. Brumen, R. Heinrich, S. Svetina, and B. Žekš. 1992. Nearly spherical vesicle shapes calculated by use of spherical harmonics: axisymmetric and nonaxisymmetric shapes and their stability. *J. Phys. II France.* 2:1081–1108.

Heinrich, V., S. Svetina, and B. Žekš. 1993. Nonaxisymmetric vesicle shapes in a generalized bilayer-couple model and the transition between oblate and prolate axisymmetric shapes. *Phys. Rev. E.* 48:3112–3123.

Heinrich, V., and R. E. Waugh. 1996. A piconewton force transducer and its application to measurement of the bending stiffness of phospholipid membranes. *Ann. Biomed. Eng.* 24:595–605.

Heinrich, V., F. Sevšek, S. Svetina, and B. Žekš. 1997. Large deviations of the average shapes of vesicles from equilibrium: effects of thermal fluctuations in the presence of constraints. *Phys. Rev. E.* 55:1809–1818.

Helfrich, W. 1973. Elastic properties of lipid bilayers: theory and possible experiments. *Z. Naturforsch.* 28c:693–703.

Helfrich, W. 1974. Blocked lipid exchange in bilayers and its possible influence on the shape of vesicles. *Z. Naturforsch.* 29c:510–515.

Hochmuth, R. M., N. Mohandas, and P. L. Blackshear, Jr. 1973. Measurement of the elastic modulus for red cell membrane using a fluid mechanical technique. *Biophys. J.* 13:747–762.

Hochmuth, R. M., H. C. Wiles, E. A. Evans, and J. T. McCown. 1982. Extensional flow of erythrocyte membrane from cell body to elastic tether. II. Experiment. *Biophys. J.* 39:83–89.

Hochmuth, R. M., J.-Y. Shao, J. Dai, and M. P. Sheetz. 1996. Deformation and flow of membrane into tethers extracted from neuronal growth cones. *Biophys. J.* 70:358–369.

Hotani, H., and H. Miyamoto. 1990. Dynamic features of microtubules as visualized by dark-field microscopy. *Adv. Biophys.* 26:135–156.

Hwang, W. C., and R. E. Waugh. 1997. Energy of dissociation of lipid bilayer from the membrane skeleton of red blood cells. *Biophys. J.* 72:2669–2678.

Jarić, M., U. Seifert, W. Wintz, and M. Wortis. 1995. Vesicular instabilities: The prolate-to-oblate transition and other shape instabilities of fluid bilayer membranes. *Phys. Rev. E.* 52:6623–6634.

Käs, J., E. Sackmann, R. Podgornik, S. Svetina, and B. Žekš. 1993. Thermally induced budding of phospholipid vesicles–a discontinuous process. *J. Phys. II France.* 3:631–645.

Kuchnir Fygenson, D., M. Elbaum, B. Shraiman, and A. Libchaber. 1997a. Microtubules and vesicles under controlled tension. *Phys. Rev. E.* 55: 850–859.

Kuchnir Fygenson, D., J. F. Marko, and A. Libchaber. 1997b. Mechanics of microtubule-based membrane extension. *Phys. Rev. Lett.* 79: 4497–4500.

Lipowsky, R. 1991. The conformation of membranes. *Nature.* 349: 475–481.

Miao, L., U. Seifert, M. Wortis, and H.-G. Döbereiner. 1994. Budding transitions of fluid-bilayer vesicles: the effect of area-difference elasticity. *Phys. Rev. E.* 49:5389–5407.

Podgornik, R., S. Svetina, and B. Žekš. 1995. Parametrization invariance and shape equations of elastic axisymmetric vesicles. *Phys. Rev. E.* 51:544–547.

Raphael, R. M., and R. E. Waugh. 1996. Accelerated interleaflet transport of phosphatidylcholine molecules in membranes under deformation. *Biophys. J.* 71:1374–1388.

Sackmann, E. 1995. Physical basis of self-organization and function of membranes: physics of vesicles. *In* Handbook of Biological Physics, Vol. 1. R. Lipowsky, and E. Sackmann, editors. Elsevier Science B.V., Amsterdam. 213–304.

Seifert, U., K. Berndl, and R. Lipowsky. 1991. Shape transformations of vesicles: phase diagram for spontaneous-curvature and bilayer-coupling model. *Phys. Rev. A.* 44:1182–1202.

Seifert, U., L. Miao, H.-G. Döbereiner, and M. Wortis. 1992. Budding transition for bilayer fluid vesicles with area-difference elasticity. *In* The Structure and Conformation of Amphiphilic Membranes. R. Lipowsky, D. Richter, and K. Kremer, editors. Springer-Verlag, Berlin, Heidelberg. 93–96.

Seifert, U. 1997. Configurations of fluid membranes and vesicles. *Adv. Phys.* 46:13–137.

Song, J. B., and R. E. Waugh. 1993. Bending rigidity of SOPC membranes containing cholesterol–brief communication. *Biophys. J.* 64:1967–1970.

Svetina, S., and B. Žekš. 1989. Membrane bending energy and shape determination of phospholipid vesicles and red blood cells. *Eur. Biophys. J.* 17:101–111.

Svetina, S., and B. Žekš. 1990. The mechanical behaviour of cell membranes as a possible physical origin of cell polarity. *J. Theor. Biol.* 146:115–122.

Svetina, S., B. Božič, J. Song, R. E. Waugh, and B. Žekš. 1992. Phospholipid membrane local and non-local bending moduli determined by tether formation from aspirated vesicles. *In* The Structure and Conformation of Amphiphilic Membranes. R. Lipowsky, D. Richter, and K. Kremer, editors. Springer-Verlag, Berlin, Heidelberg. 154–157.

Svetina, S., and B. Žekš. 1992. Elastic properties of closed layered membranes and equilibrium shapes of phospholipid vesicles. *In* Proceedings of the Eleventh School on Biophysics of Membrane Transport. J. Kuczera and S. Przestalski, editors. Agricultural University of Wrocław, Poland. 115–140.

Svetina, S., and B. Žekš. 1996. Elastic properties of closed bilayer membranes and the shapes of giant phospholipid vesicles. *In* Handbook of Nonmedical Applications of Liposomes, Vol. 1. D. D. Lasic and Y. Barenholz, editors. CRC Press, Boca Raton, New York, London, Tokyo. 13–42.

Svetina, S., B. Žekš, R. E. Waugh, and R. M. Raphael. 1998. Theoretical analysis of the effect of the transbilayer movement of phospholipid molecules on the dynamic behavior of a microtube pulled out of an aspirated vesicle. *Eur. Biophys. J.* 27:197–209.

Umeda, T., H. Nakajima, and H. Hotani. 1998. Theoretical analysis of shape transformations of liposomes caused by microtubule assembly. *J. Phys. Soc. Japan.* 67:682–688.

Waugh, R. E. 1982. Surface viscosity measurements from large bilayer vesicle tether formation. II. Experiments. *Biophys. J.* 38:29–37.

Waugh, R. E., J. Song, S. Svetina, and B. Žekš. 1992. Monolayer coupling and curvature elasticity in bilayer membranes by tether formation from lecithin vesicles. *Biophys. J.* 61:974–982.

Waugh, R. E., and R. G. Bauserman. 1995. Physical measurement of bilayer-skeletal separation forces. *Ann. Biomed. Eng.* 23:308–321.

Wiese, W., W. Harbich, and W. Helfrich. 1992. Budding of lipid bilayer vesicles and flat membranes. *J. Phys.: Condens. Matter.* 4:1647–1657.

Wintz, W., H.-G. Döbereiner, and U. Seifert. 1996. Starfish vesicles. *Europhys. Lett.* 33:403–408.